JACS
JOURNAL OF THE AMERICAN CHEMICAL SOCIETY

Article

pubs.acs.org/JACS

Improved Understanding of the Electronic and Energetic Landscapes of Perovskite Solar Cells: High Local Charge Carrier Mobility, Reduced Recombination, and Extremely Shallow Traps

Hikaru Oga,[†] Akinori Saeki,*[,†,‡] Yuhei Ogomi,[§,∥] Shuzi Hayase,[§,∥] and Shu Seki*[,†]

[†]Department of Applied Chemistry, Graduate School of Engineering, Osaka University, 2-1 Yamadaoka, Suita, Osaka 565-0871, Japan

[‡]Japan Science and Technology Agency (JST)-PRESTO, 4-1-8 Honcho, Kawaguchi, Saitama 332-0012, Japan

[§]Graduate School of Life Science and Systems Engineering, Kyushu Institute of Technology, 2-4 Hibikino, Wakamatsu-ku, Kitakyushu, Fukuoka 808-0196, Japan

[∥]CREST, Japan Science and Technology Agency (JST), 4-1-8 Honcho, Kawaguchi, Saitama 332-0012, Japan

Supporting Information

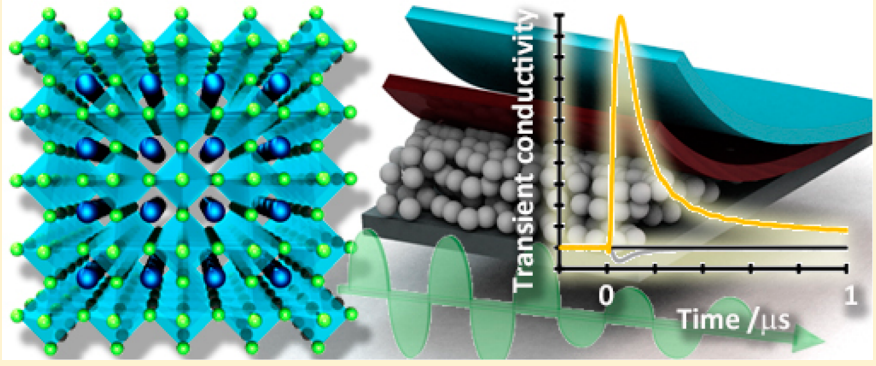

ABSTRACT: The intriguing photoactive features of organic−inorganic hybrid perovskites have enabled the preparation of a new class of highly efficient solar cells. However, the fundamental properties, upon which the performance of these devices is based, are currently under-explored, making their elucidation a vital issue. Herein, we have investigated the local mobility, recombination, and energetic landscape of charge carriers in a prototype $CH_3NH_3PbI_3$ perovskite (PVK) using a laser-flash time-resolved microwave conductivity (TRMC) technique. PVK was prepared on mesoporous TiO_2 and Al_2O_3 by one or two-step sequential deposition. PVK on mesoporous TiO_2 exhibited a charge carrier mobility of 20 $cm^2\ V^{-1}\ s^{-1}$, which was predominantly attributed to holes. PVK on mesoporous Al_2O_3, on the other hand, exhibited a 50% lower mobility, which was resolved into balanced contributions from both holes and electrons. A general correlation between crystal size and mobility was revealed irrespective of the fabrication process and underlying layer. Modulating the microwave frequency from 9 toward 23 GHz allowed us to determine the intrinsic mobilities of each PVK sample (60−75 $cm^2\ V^{-1}\ s^{-1}$), which were mostly independent of the mesoporous scaffold. Kinetic and frequency analysis of the transient complex conductivity strongly support the superiority of the perovskite, based on a significant suppression of charge recombination, an extremely shallow trap depth (10 meV), and a low concentration of these trapped states (less than 10%). The transport mechanism was further investigated by examining the temperature dependence of the TRMC maxima. Our study provides a basis for understanding perovskite solar cell operation, while highlighting the importance of the mesoporous layer and the perovskite fabrication process.

1. INTRODUCTION

Organometallic lead halide perovskites, first introduced as sensitizers in dye-sensitized solar cells in 2009,[1] have shown great promise since the advent of fully solid-state mesoporous superstructure solar cells.[2,3] These solar cells mainly consist of an electron transport layer (ETL) of mesoporous titanium dioxide or alumina (mp-TiO_2 or mp-Al_2O_3), a methylammonium lead halide ($CH_3NH_3PbX_3$) perovskite layer, and a spiro-OMeTAD hole transport layer (HTL). The perovskite layer plays a central role in photoabsorption and charge separation.[4,5] In addition to its unprecedented ambipolar charge transport,[3,6,7] its low energy loss between the optical bandgap and open circuit voltage (V_{oc}) has enabled notable improvements in the photovoltaic output, leading to an impressive boost in power conversion efficiencies (PCE), of solar cells contained these layers.[8−11] This has also triggered various investigations of potential device materials[12−14] and processes,[15−17] and theoretical calculations.[18−20] However, the fundamental opto-electronic aspects underlying the operation of this type of solar

Received: July 9, 2014
Published: September 4, 2014

   dx.doi.org/10.1021/ja506936f | J. Am. Chem. Soc. 2014, 136, 13818−13825

cell remain elusive, rendering this theme prevalent in the study of the dynamics of excitons and charge carriers by ultrafast transient absorption,[2,3,6,7,21] fluorescence lifetime,[6,7] impedance spectroscopy,[22,23] and time-resolved terahertz (THz)[24] and gigahertz (GHz)[25,26] conductivity.

In this work, the optoelectronic properties of the benchmark iodide perovskite $CH_3NH_3PbI_3$, hereafter abbreviated as PVK, were investigated by time-resolved microwave conductivity (TRMC). TRMC allows noncontact evaluation of the dynamics of photogenerated charge carriers using an alternating-current electromagnetic wave with nanosecond time resolution.[27,28] We focused on the role of the underlying mp-TiO_2 or mp-Al_2O_3 scaffolds on variations in local charge carrier mobility and recombination kinetics, which are intimately associated with the crystallographic composition of PVK and any residual PbI_2 present after its conversion to PVK. In particular, the complex transient conductivity modulated by the excitation laser power and microwave frequency from 9 to 23 GHz revealed that PVK on mp-TiO_2 has an extremely high charge carrier mobility and low trap density. The good correlation between the TRMC results and device performance highlights the importance of understanding the photophysics of these devices, which is greatly affected by the delicate film processing and underlying scaffolds.

2. RESULTS AND DISCUSSION

2.1. Local Charge Carrier Mobility at 9 GHz. We prepared the following six samples on quartz plates: pure PVK, bare mesoporous (mp)-TiO_2 (TiO_2), PVK on mp-TiO_2 (PVK/TiO_2) or mp-Al_2O_3 (PVK/Al_2O_3), and spiro-OMeTAD[29] coated PVK on both mp-TiO_2 and mp-Al_2O_3 (Spiro/PVK/TiO_2 and Spiro/PVK/Al_2O_3). Note that the insulating mp-Al_2O_3 layer was confirmed to be completely unresponsive to laser-flash TRMC. Figure 1a shows the maximum $\phi\Sigma\mu$ ($\phi\Sigma\mu_{max}$) of the TRMC transients, monitored at 9.1 GHz, versus the incident laser intensity, I_0, from 10^{10} to 10^{15} photons cm^{-2}. The transient decays of $\phi\Sigma\mu$ at various I_0 values are displayed in Figure S1 of the Supporting Information. ϕ and $\Sigma\mu$ are the charge carrier generation efficiency and the sum of the positive and negative charge carrier mobilities ($\mu_+ + \mu_-$), respectively. The PVK samples, regardless of the presence of mp-TiO_2 and mp-Al_2O_3, exhibited exceptionally high $\phi\Sigma\mu_{max}$ values in comparison to bare mp-TiO_2 and a typical bulk heterojunction (a blend of poly(3-hexylthiophene) (P3HT) and phenyl-C_{61}-butyric acid methyl ester (PCBM)). For both PVK and PVK/TiO_2, $\phi\Sigma\mu_{max}$ increased with decreasing I_0 as a result of reduced charge recombination at lower I_0. Surprisingly, their $\phi\Sigma\mu_{max}$, also regarded as their minimum mobility, reached ca. 20 $cm^2\ V^{-1}\ s^{-1}$ at the lowest I_0 (~10^{10} photons cm^{-2}), indicating that in both of these samples, PVK was behaving as an excellent photoactive layer (Table 1). This value exceeded those of P3HT:PCBM (0.22 $cm^2\ V^{-1}\ s^{-1}$)[30] and bare mp-TiO_2 (0.066 $cm^2\ V^{-1}\ s^{-1}$, consistent with literature values[31,32]) by several orders of magnitude. $\phi\Sigma\mu_{max}$ of PVK/Al_2O_3 was ca. 10 $cm^2\ V^{-1}\ s^{-1}$ at the lowest I_0, which is close to the THz local mobilities of PVK/Al_2O_3 determined by Herz et al. (8.1 $cm^2\ V^{-1}\ s^{-1}$)[24] and Ponseca et al. (20 $cm^2\ V^{-1}\ s^{-1}$).[26] Though for a more exact comparison, we should state that the mobility of our PVK/Al_2O_3 was half of that found in the work of Ponseca et al.[26] In contrast, our value for PVK/TiO_2 (20 $cm^2\ V^{-1}\ s^{-1}$) was 2.7 times larger than that of the latter report (Ponseca et al., 7.5 $cm^2\ V^{-1}\ s^{-1}$),[26] while the mobilities of pure PVK in both studies were the same (20 $cm^2\ V^{-1}\ s^{-1}$).[26] It should be noted that the PVK layers of the previous THz studies were prepared by a single step method from a solution of PbI_2 and excess CH_3NH_3I (e.g., in a ratio of 1:3),[24,26] while our preparation adopted a two-step sequential deposition method using a DMF solution of PbI_2 followed by dipping into an IPA solution of CH_3NH_3I.[10] In the early days of perovskite solar cell research, PVK/Al_2O_3 devices based on the one-step procedure provided higher device outputs than PVK/TiO_2 devices,[3] in accordance with the THz mobilities reported by Ponseca et al.[26] On the other hand, recent PVK/TiO_2 devices with enhanced PCE and

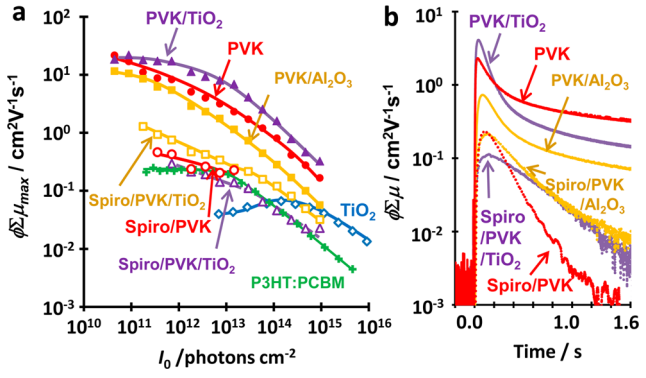

Figure 1. (a) $\phi\Sigma\mu_{max}$ of 9 GHz TRMC transients of perovskite (PVK) films plotted against the incident laser photon density, I_0. For reference, data from P3HT:PCBM (1:1 weight fraction)[30] and mesoporous TiO_2 films are also shown. The lines are visual guides. (b) $\phi\Sigma\mu_{max}$ transients of PVK on mesoporous scaffolds with (dotted line) or without (solid line) spiro-OMeTAD at I_0 = 1.5 (PVK) or 2.9 × 10^{13} (others) photons cm^{-2}.

Table 1. TRMC Studies of the Electronic Properties of $CH_3NH_3PbI_3$ Perovskite Films Prepared by a Two-Step Method

	pure PVK	PVK/TiO_2	PVK/Al_2O_3
$\Sigma\mu$ ($cm^2\ V^{-1}\ s^{-1}$)[a]	20	20	10
μ_+ ($cm^2\ V^{-1}\ s^{-1}$)[a]	17	19	7
μ_- ($cm^2\ V^{-1}\ s^{-1}$)[a]	3	0.6	3
k_2($cm^3\ s^{-1}$)[b]	8×10^{-12}	4×10^{-13}	2×10^{-12}
k_2/k_{Lg}[c]	3×10^{-5}	1×10^{-6}	7×10^{-5}
τ''/τ'[d]	1–0.7	0.9	0.8
$\phi\Sigma\mu$ ($cm^2\ V^{-1}\ s^{-1}$)[e]	65	75	60
c[f]	−0.86	−0.89	−0.91
E_T (meV)[f]	10 ± 1	10 ± 1	10 ± 1
f_{trap}[f]	0.03 ± 0.01 (0.1 ± 0.02)	0.03 ± 0.01	0.08 ± 0.03

[a]The minimum 9 GHz mobility observed at 4.4×10^{10} photons cm^{-2}, λ_{ex} = 355 nm. The hole and electron mobilities were separated on the basis of $\phi\Sigma\mu_{max}$ suppression by a spiro-OMeTAD coating. [b]The second-order rate obtained by analyzing 9 GHz transient conductivities at $I_0 = 4.7 \times 10^{14}$ photons cm^{-2}. [c]A k_{Lg} of 3.0×10^{-7} $cm^3\ s^{-1}$ (see text for the estimation) was assumed for all of the samples. [d]The ratio of the half-life of the real to imaginary conductivity transients at 9 GHz. Pure PVK shows a characteristic dependence on I_0. The others are almost constant. [e]The minimum 23 GHz mobility averaged at low I_0 ((4.4–18) × 10^{10} photons cm^{-2}). [f]Parameters used in the Drude-Smith/Drude-Zener model. This analysis was applied to the end-of-pulse conductivity values at the lowest I_0 (4.4×10^{10} photons cm^{-2}), except for the value in brackets of pure PVK ($I_0 = 7.3 \times 10^{12}$ photons cm^{-2}, where the τ''/τ' is at a minimum).

dx.doi.org/10.1021/ja506936f | J. Am. Chem. Soc. 2014, 136, 13818–13825

reproducibility have been fabricated using the two-step method.[10] To provide control data, we performed TRMC of one-step PVK samples prepared from DMF solution of CH_3NH_3I and PbI_2 (1:1) mixture and found that the mobilities were 17 and 4.3 $cm^2\ V^{-1}\ s^{-1}$ for of PVK/TiO_2 and PVK/Al_2O_3, respectively (Supporting Information Figure S2). They are lower than the corresponding PVK on mesoporous scaffold of the two-step method, underscoring the superiority of the two-step PVK/TiO_2. In our device characterization, the two-step PVK/TiO_2 indeed demonstrated a higher efficiency (PCE = 9.6%, short-circuit current density (J_{sc}) = 19.2 mA cm^{-2}, V_{oc} = 0.90 V, and fill factor (FF) = 0.56) than PVK/Al_2O_3 (PCE = 1.9%, J_{sc} = 4.5 mA cm^{-2}, V_{oc} = 0.95 V, FF = 0.44, Supporting Information Figure S3), in line with the TRMC mobility trends reported here. The local mobility of charge carriers is not, of course, the sole determinant governing device output. However, the observed qualitative correlation between the device output and local mobility is worth mentioning. Thickness variation (260−420 nm) and resultant absorbance difference of PVK are not significant (Supporting Information Figure S4).

The application of HTL (spiro-OMeTAD) top-coatings onto PVK, PVK/TiO_2 and PVK/Al_2O_3 led to a significant suppression of $\phi\Sigma\mu_{max}$ (Figure 1a). PVK and PVK/TiO_2 underwent a large decrease of 1−2 orders of magnitude (×1/6 for PVK and 1/30 for PVK/TiO_2 averaged over all I_0), while the decrease was more moderate for PVK/Al_2O_3 (×1/3 on average) when the HTL coating was present. Supposing that hole mobility in spiro-OMeTAD is negligibly small (probable because its time-of-flight mobility is 2×10^{-4} $cm^2\ V^{-1}\ s^{-1}$)[33] and that hole transfer from PVK to HTL occurs very quickly (also probable because time constants of 16 ns for $CH_3NH_3PbI_2Cl$[34] and ca. 10 ns for two-step PVK[25] have been observed), we can deduce that the hole is the primary charge carrier contributing to the TRMC mobility in PVK (μ_+ = 17 $cm^2\ V^{-1}\ s^{-1}$ and μ_- = 3 $cm^2\ V^{-1}\ s^{-1}$) and PVK/TiO_2 (μ_+ = 19 $cm^2\ V^{-1}\ s^{-1}$ and μ_- = 0.6 $cm^2\ V^{-1}\ s^{-1}$). These assumptions are validated by the decay profiles, which show that the HTL coating significantly quenched the PVK conductivity on a long time scale (>ca. 1 μs, Figure 1b). Furthermore, such a low electron mobility is consistent with the equal $\Sigma\mu$ values that were observed for PVK and PVK/TiO_2 despite the reported instantaneous electron injection from PVK into mp-TiO_2.[25] Notably, the μ_- in PVK/TiO_2 and PVK (0.6 and 3 $cm^2\ V^{-1}\ s^{-1}$) shows good consistency with the electron mobilities of 0.66 and 1.39 $cm^2\ V^{-1}\ s^{-1}$ reported for pure PVK on glass, on the basis of fluorescence lifetime spectroscopy studies by Snaith et al.[6] and Xing et al.,[7] respectively.[35] Despite the unbalanced mobility ($\mu_+/\mu_- \approx 30$) and its inferior μ_-, the PVK/TiO_2 device fabricated by the two-step method worked efficiently. In sharp contrast, PVK/Al_2O_3 had more comparable mobilities with μ_+ = 7 $cm^2\ V^{-1}\ s^{-1}$ and μ_- = 3 $cm^2\ V^{-1}\ s^{-1}$. Due to its electron transport capability, TiO_2 offers a bypass for electrons to travel toward the cathode, which can compensate for the low electron mobility in the perovskite phase. Conversely, electrically inert mp-Al_2O_3 can neither receive nor transport electrons, the perovskite crystallites must, therefore, contact the underlying substrate through the jungle-like mesoporous alumina. This situation, therefore, certainly favors complete conversion of PbI_2 to PVK in the deep mp-Al_2O_3 region, which might be more suited to a one-step procedure than a two-step procedure. In addition to the different contribution of μ_+ and μ_- dependent on the underlying scaffold, the transient conductivity of Spiro/PVK/TiO_2 decays slower than those of Spiro/PVK and Spiro/PVK/Al_2O_3, which is relevant to the improved device output of PVK/TiO_2.

2.2. Crystalline Quality Assessment by X-ray Diffraction and Morphology. X-ray diffraction (XRD) spectra were measured (Figure 2) to obtain crystallographic information about the perovskite on the mesoporous scaffolds. The spectra were clearly resolved for 2θ = 10−45°, and the peaks were readily assigned to PVK ($CH_3NH_3PbI_3$), PbI_2, and TiO_2 according to the literature.[3,10,36] Hereafter, we concentrated our attention on the two peaks at the low diffraction angles of 2θ = 12.7° (due to the (001) plane of the hexagonal 2H polytype phase of PbI_2) and 14.1° (due to the (110) plane of the tetragonal phase of PVK).[10] Although both of these peaks appeared in all of the spectra of the samples containing PVK, their relative peak intensities varied with changes to the underlying mesoporous layer. The PbI_2 peak at 12.7° was more pronounced in the PVK/TiO_2 spectra, where it was about 2−3 times higher than the PVK peak at 14.1°. Conversely, the PbI_2 peak was less pronounced (only about half as high) than the PVK peak in PVK/Al_2O_3. However, the amplitude of the PVK peak in PVK/Al_2O_3 was comparatively small, despite the substantially reduced PbI_2 peak. This indicates that more unconverted PbI_2 remained in the PVK/TiO_2 samples than in PVK/Al_2O_3. On the contrary, those samples prepared by one-step method completely quenched the PbI_2 peaks irrespective of the scaffold, leaving only the PVK peaks. Nonetheless, the solar cells based on one-step method have a lower PCE and reproducibility[3] with a large hysteresis on voltage sweep.[37,38] The crystal size correlating with the slow polarization of perovskite was proposed as a possible cause of hysteresis by Park et al., where the hysteresis was mitigated by the increase in crystal size and the use of mesoporous TiO_2.[39]

Atomic force microscopy (AFM) of our perovskite indicates that the crystal size of two-step PVK/TiO_2 (420 ± 50 nm) is obviously larger than that of one-step PVK/TiO_2 (300 ± 80 nm) and both PVK/Al_2O_3 (70−100 nm) as shown in Figure 3a−e. Importantly, Figure 3f presents a general correlation with

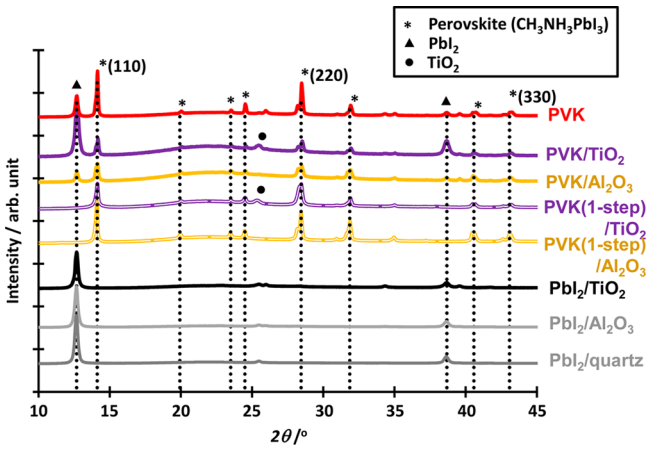

Figure 2. XRD spectra of PVK (red), PVK/TiO_2 (purple), and PVK/Al_2O_3 (yellow). The solid color lines are two-step samples, while doubled lines are one-step ones. The black and gray curves are as-spun PbI_2 on different under-layer. The peaks are assigned to $CH_3NH_3PbI_3$, PbI_2, and TiO_2 are indicated by stars, triangles, and circles, respectively.

dx.doi.org/10.1021/ja506936f | J. Am. Chem. Soc. 2014, 136, 13818−13825

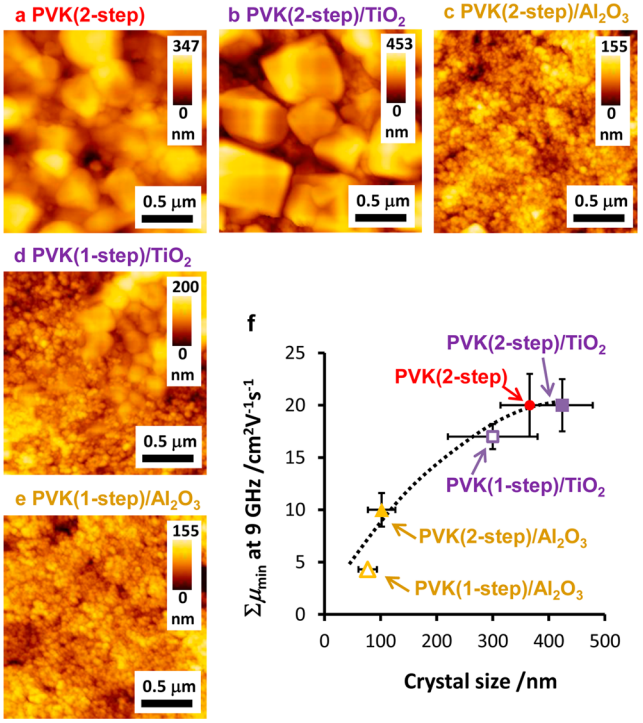

Figure 3. AFM topographic images of (a) PVK (two-step), (b) PVK/TiO_2 (two-step), (c) PVK/Al_2O_3 (two-step), (d) PVK/TiO_2 (one-step), and (e) PVK/Al_2O_3 (one-step). The image size is 2 × 2 μm^2. (f) Plot of $\Sigma\mu_{min}$ measured by TRMC at 9 GHz (Table 1) versus averaged crystal size. The dotted line is a visual guide.

the minimum mobility ($\Sigma\mu$) at 9 GHz and the crystal size, irrespective of one- and two-step methods and mesoporous scaffolds. The crystal size can be also controlled by tuning the PbI_2 concentration.[40] Our finding exemplifies the relationship between inherent charge carrier mobility (mainly hole) and crystal size of perovskite affected by the preparation process and underlayer. It is of interest to note that one-step PVK/TiO_2 contains both large and small crystals (Figure 3d). Electronic property of nanosized semiconductor such as TiO_2 nanoparticles is often susceptible to the trapping at surface defects and interstructural barrier for charge transport, which are reduced with increasing the crystal size.[31] In this work, the two-step PVK/TiO_2 having the largest size showed the highest TRMC mobility and PCE. The analogy infers that the crystal size relating to the polarization of perovskite,[39] rather than incomplete conversion of PbI_2, limits the TRMC mobility and overall device output.

Along with a respectable 15% PCE, Burschka et al. demonstrated that mp-TiO_2 facilitates the conversion of PbI_2 to the perovskite during the two-step process, because of confinement of PbI_2 within the nanoporous TiO_2 network.[10] They observed almost complete extinction of the PbI_2 peak in the XRD spectra of PVK/TiO_2. In contrast, their PVK sample without mp-TiO_2 generated intense PbI_2 peaks. The conversion of PbI_2 to PVK starts immediately after immersing a PbI_2/mp-TiO_2 film into a CH_3NH_3I solution, initially on the surfaces of PbI_2 crystallites but quickly proceeds toward the inside layer of PbI_2 at the mp-TiO_2 surface.[41] However, it is commonly recognized that prolonged immersion in the CH_3NH_3I solution deteriorates the resulting devices photovoltaic performance.[42] Therefore, as discussed above the remaining *thin* PbI_2 layer on the mp-TiO_2 surface after a short immersion (e.g., 20 s) does not crucially block the electron transfer from PVK to mp-TiO_2. It is noted that PbI_2 on its own produces a TRMC signal, but the intensity of this signal is more than 2 orders of magnitude lower than that of PVK. This is in agreement with the photocurrent/photovoltage results on PbI_2, in which the diffusion constant of charge carriers on a long-range (film thickness) is a factor of 5 smaller than that in perovskite.[43] Meanwhile, computational study suggests that the formation of the flat terminations under the PbI_2-rich condition leads to the improvement of device performance, benefited from the shallow surface state for hole transfer.[44] This is also a reasonable interpretation on the coexistence of the highest hole mobility and remaining PbI_2 in our PVK/TiO_2. However, an ideal morphology would be a dense and flat perovskite layer with large uniform domain and minimal remaining PbI_2, which was achieved via vapor deposition by Snaith et al. with 15.4% PCE.[9] Recently, Seok et al. have realized such a flat perovskite layer by solvent engineering, leading to the remarkable PCE of 16.2% with no hysteresis.[45] Compared with these state-of-the-arts[9,45] and the first two-step cell,[10] our PVK/TiO_2 contains excessive PbI_2, which might be one of the reasons for about 40% lower PCE of our device (9.6%).

From the XRD and AFM characterizations, the two-step PVK/TiO_2 has the largest crystal size and the highest amount of unconverted PbI_2. The observed general correlation between $\Sigma\mu$ and crystal size is underlined by the fact that the two-step PVK/TiO_2 shows the highest local mobility and PCE. This is presumably due to the superior electronic quality associated with perovskite polarization[39] and reduced charge trap (vide infra). The use of mp-Al_2O_3 and/or one-step procedure decreased the unconverted PbI_2 contents, while it leads to the fractionated crystals and impaired mobility.

2.3. Reduced Charge Recombination. By assuming that $\Sigma\mu$ is constant over the whole I_0 range, we analyzed the TRMC transients on the basis of first- and second-order kinetics according to previous methods.[46] Figure 4a is a plot of the

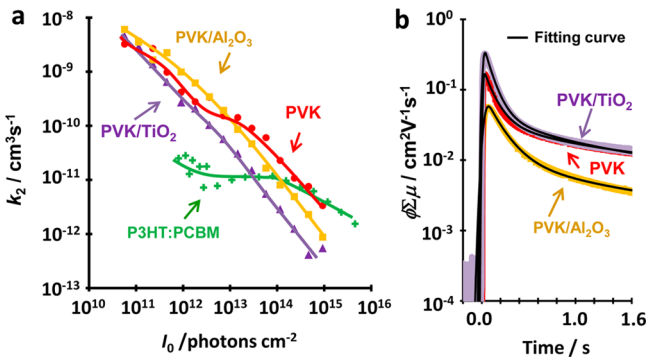

Figure 4. (a) Second-order rate (k_2) of PVK, PVK/TiO_2, PVK/Al_2O_3, and a reference P3HT:PCBM (1:1 weight fraction) as a function of laser intensity (I_0) monitored at 9 GHz. The lines are visual guides. (b) $\phi\Sigma\mu$ transients of PVK (red), PVK/TiO_2 (purple), and PVK/Al_2O_3 (orange) films at I_0 = 9.3 × 10^{14} photons cm^{-2}, along with an analytical fitting curve (black line).

second-order bimolecular recombination rate k_2 as a function of I_0. The accuracy of this analysis is established by the perfect match between the experimental decay and the analytical fitting curve convoluted by a response function (Figure 4b). In Figure 4a, the pure perovskite film showed a large exponential reduction of k_2 with increasing I_0. At the I_0 corresponding to a

dx.doi.org/10.1021/ja506936f | J. Am. Chem. Soc. 2014, 136, 13818−13825

charge carrier concentration of 10^{17} cm^{-3} at the pulse end (a typical charge carrier density under 1 sun illumination), k_2 was as low as 8×10^{-12} cm^3 s^{-1} (Table 1) for pure PVK. This is 4–5 orders of magnitude lower than the Langevin rate (k_{Lg}) of 3.0×10^{-7} cm^3 s^{-1} calculated on the basis of recombination in a homogeneous system.[47] It is noteworthy that the ratio k_2/k_{Lg} is in good accordance with a previous THz conductivity study.[24] The k_2 of PVK/TiO_2 was a further order of magnitude lower than k_{Lg} at 4×10^{-13} cm^3 s^{-1}. This can be explained by electron injection into the TiO_2 and a deceleration of back electron transfer. P3HT:PCBM also demonstrates a significant inhibition of charge recombination by 2–3 orders of magnitude, i.e., $k_2 = 1 \times 10^{-11}$ cm^3 s^{-1} and $k_{Lg} = 1.7 \times 10^{-9}$ cm^3 s^{-1}. The k_2/k_{Lg} of P3HT:PCBM was in good agreement with literature values,[48] and can be explained by the inhomogeneous charge carrier transport of holes in the donor phase (P3HT) and electrons in the acceptor phase (PCBM), leading to a reduction in recombination at the donor–acceptor interface. PVK does not contain two such spatially separated phases, but its valence band (the hybridization of the 6s-orbitals of lead and 5p-orbitals of iodine) and conduction band (the hybridization of the 6p-orbitals of lead) are orthogonal in space,[17,18] which could be responsible for the reduced recombination rate. It has also been suggested that the presence of ferroelectric domains may assist charge separation and reduce recombination.[49] The excellent photovoltaic performance of the perovskite framework is, therefore, clearly due to its reduced charge recombination rate over long time scales.

2.4. Kinetics of the Complex Conductivity Indicative of a Low Trap Density. To investigate the electronic quality of the perovskite films, their complex transient conductivities, composed of real ($\Delta\sigma$) and imaginary ($\Delta\sigma''$) parts, were examined using our previously reported technique,[32] which has already been applied to investigate charge trapping processes in TiO_2 nanoparticles. A free charge carrier has larger real and smaller imaginary components than a shallowly trapped one. Figure 5 shows the ratio of the real to imaginary conductivity transient half-lives, τ''/τ', plotted against I_0. The τ''/τ' ratio is a simple indicator of the kinetic difference between $\Delta\sigma'$ and $\Delta\sigma''$, a τ''/τ' ratio of unity would, therefore, indicate that the real and imaginary conductivities decay in the same fashion.[32] For example, P3HT:PCBM exhibited identical time profiles for the real and imaginary conductivities (therefore $\tau''/\tau' = 1.0$),[32] and, subsequently, bimolecular charge recombination without temporal trapping was identified as the deactivation pathway; this has been independently confirmed by transient absorption spectroscopy.[50] The case $\tau''/\tau' < 1$ corresponds to a faster decay of the imaginary conductivity than the real conductivity, suggesting that multiple transient species making different contributions to the real and imaginary conductivities are involved in the complex conductivity. We have, previously, rationalized that the τ''/τ' ratio of 0.2–0.4 observed for TiO_2 nanoparticles resulted from the evolution of trap depths (E_T) as a function of time and the relative populations of free and shallowly trapped electrons.[32] A small τ''/τ' ratio was also observed for mp-TiO_2 (0.6–0.7) in the present study. For the perovskite films, the τ''/τ' ratio of PVK/TiO_2 remained high, at 0.9 over the whole I_0 range, highlighting the presence of a small population of shallowly trapped charge carriers. It should be noted that the E_T of these shallowly trapped carriers was less than 0.3 eV, typically about 0.01–0.12 eV, and deeply trapped charges (E_T > 0.3 eV) are too immobile to contribute to the GHz conductivity. The τ''/τ' ratio of PVK/Al_2O_3 decreased to 0.8, on average, concomitant with a weak decreasing tendency with increasing I_0. Note that for pure PVK, the τ''/τ' ratio had a strong convex dependence on I_0. The τ''/τ' ratio was close to 1 at low I_0 (10^{10} photons cm^{-2}), it then rapidly decreased to a minimum of 0.7 at 10^{12} photons cm^{-2} and finally increased to 0.8. Interestingly, this convex trend is similar to the relative intensities of $\phi\Sigma\mu_{max}$ between pure PVK and PVK/TiO_2, as shown in Figure 1a. Although they both exhibited a $\phi\Sigma\mu_{max}$ of 20 cm^2 V^{-1} s^{-1} at the lowest I_0, the $\phi\Sigma\mu_{max}$ of PVK decreased more rapidly than that of PVK/TiO_2 with increasing I_0. The $\phi\Sigma\mu_{max}$ of PVK was reduced to as much as 40% of that of PVK/TiO_2. This difference was slightly mitigated at high I_0 where it was reduced to 50–60%. From this observation, we expect the charge carrier mobility in pure PVK was greatly impaired by the presence of shallowly trapped states, which resulted from the poor formation of PbI_2 crystallites on a flat substrate.[10] A similar scenario has been suggested in another report, which indicated that the presence of a thin mesoporous interlayer is responsible for reducing the exciton binding energy of the perovskite and increasing the surface effects (structurally and electronically) by tuning the perovskite crystal size.[51]

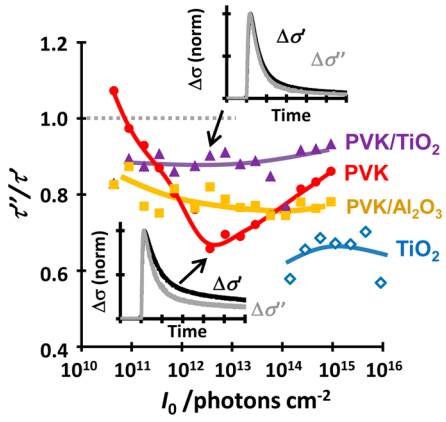

Figure 5. Half-life ratio of imaginary (τ'') to real (τ') transient conductivities monitored at 9 GHz for various laser intensities, I_0. The inset shows the normalized decay profiles of the real and imaginary conductivities ($\Delta\sigma'$, black line, and $\Delta\sigma''$, gray line) for the points indicated by the arrows. The gray dotted line represents $\tau''/\tau' = 1$ (i.e., the identical decay of $\Delta\sigma'$ and $\Delta\sigma''$). The colored lines are visual guides unless otherwise noted.

2.5. Frequency Modulation up to 23 GHz: High Mobility and Shallow Trap Depth. Finally, we performed frequency-modulated TRMC studies at 9, 15, and 23 GHz. Figure 6a shows that $\phi\Sigma\mu_{max}$ increased greatly with increasing frequency, rising by a factor of 3 to 6 (all kinetics are given in Supporting Information Figure S5). At 23 GHz under the lowest I_0 excitation, the $\phi\Sigma\mu_{max}$ values of PVK, PVK/TiO_2, and PVK/Al_2O_3 were between 60 and 75 cm^2 V^{-1} s^{-1} (see the inset of Figure 6a and Table 1). The notable increase in the minimum mobility with increasing frequency was mainly due to an increase in ϕ, which was probably constant at low I_0 because of the improved time resolution. This was strongly corroborated by the flat dependence of $\phi\Sigma\mu_{max}$ on I_0 at low I_0 values, which is more obvious at 23 GHz than at 9 GHz. Emphasis should be given to the observation that the high TRMC mobility measured for PVK correlates with the electron mobility of a polycrystalline PVK sample (66 cm^2 V^{-1} s^{-1}) estimated by Hall effect measurements at room temperature.[52]

dx.doi.org/10.1021/ja506936f | J. Am. Chem. Soc. 2014, 136, 13818–13825

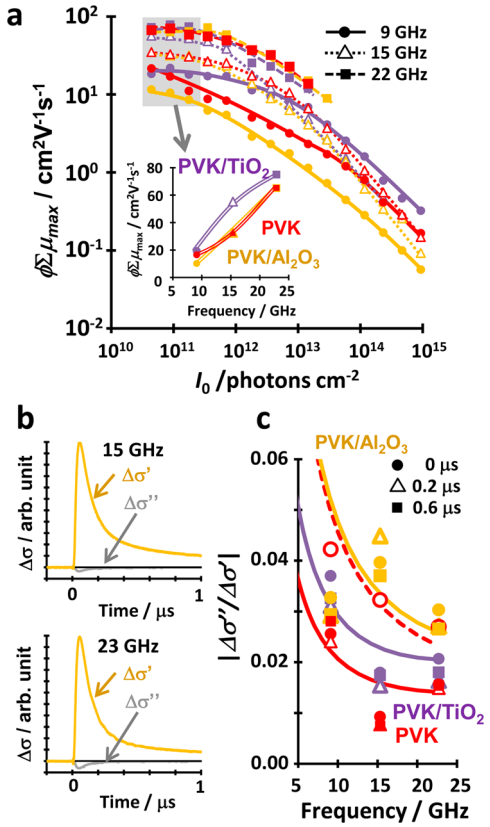

Figure 6. (a) $\phi\Sigma\mu_{max}$ dependence on I_0 for PVK/TiO_2 (purple) and PVK/Al_2O_3 (orange) at different microwave frequencies (closed circles, 9 GHz; open triangles:, 15 GHz; closed squares, 23 GHz). The inset shows $\phi\Sigma\mu_{max}$ plotted against frequency and averaged over the three points at the lowest I_0 (gray-meshed area). (b) Transient conductivities of PVK/Al_2O_3 monitored at 15 GHz (upper panel) and 23 GHz (lower panel) at $I_0 = 3.6 \times 10^{12}$ photons cm^{-2}. The orange and gray curves are the real and imaginary decays. (c) Frequency-modulated absolute values of $\Delta\sigma''/\Delta\sigma'$; the closed circles, open triangles, and closed squares represent 0, 0.2, and 0.6 μs delays, respectively, after the peak and under an excitation of $I_0 = 4.4 \times 10^{10}$ photons cm^{-2}. The solid lines are analytical curves based on a combined Drude-Smith/Drude-Zener model. The open red circles and the dashed red line represent the 0 μs delay data and the analysis results under an excitation of $I_0 = 7.3 \times 10^{12}$ photons cm^{-2}, respectively.

The complex transient conductivities of PVK/Al_2O_3 at 15 and 23 GHz are displayed in Figure 6b. The amplitude of the positive real conductivity ($\Delta\sigma'$) is about 30 times that of the negative imaginary component ($\Delta\sigma''$), irrespective of the microwave frequency. The decay speed of $\Delta\sigma''$ is slightly higher than that of $\Delta\sigma'$, as discussed for the 9 GHz case (Figure 5). In Figure 6c, the absolute ratio of the complex conductivity $|\Delta\sigma''/\Delta\sigma'|$ is plotted against the microwave frequency at different delay times (0, 0.2, and 0.6 μs), allowing to compensate for the time resolution mismatch at each frequency. $|\Delta\sigma''/\Delta\sigma'|$ ratios were analyzed using a combined Drude-Smith/Drude-Zener model, which can provide a wealth of information on the evolution of E_T as a function of time and the population of shallowly trapped charge carriers ($0 < f_{trap} < 1$).[32] The experimental TRMC mobility at 23 GHz was used as the intrinsic mobility in this analysis. An effective mass of 0.29 m_e was employed, which is obtained by theoretical calculations for the hole ($m_h^* = 0.29\ m_e$) and electron ($m_e^* = 0.23\ m_e$).[19]

As a consequence, a small E_T of 10 ± 1 meV was determined for all of the perovskite samples (Table 1). This is much lower than the exciton binding energy (50 meV) of PVK[51] and our previous results for TiO_2 nanoparticles (110 meV) and P3HT:PCBM (60 meV).[32]

Moreover, we observed low f_{trap} values for PVK and PVK/TiO_2 (0.03 ± 0.01) and PVK/Al_2O_3 (0.08 ± 0.03). Interestingly, the f_{trap} of PVK at 0 μs increased to 0.1 ± 0.02 at intermediate I_0 (7.3×10^{12} photons cm^{-2}, Table 1), which coincided with the I_0 that resulted in the minimum τ''/τ' ratio, as shown in Figure 5. These results imply that the local mobility of shallowly trapped charge carriers is strongly modulated by the charge carrier density. E_T and f_{trap} fluctuated only within the limits of experimental error at each delay time, suggesting an absence of apparent trapping and/or selective recombination processes on a long time scale.[32] These results support the electronically robust nature of PVK/TiO_2, in sharp contrast to that of TiO_2 nanoparticles (f_{trap} = 0.8–0.98) and P3HT:PCBM (f_{trap} = 0.25).[32] The conductivity transient maxima of PVK/TiO_2 at low temperatures shown in Figure 7 revealed a $T^{-1.4}$

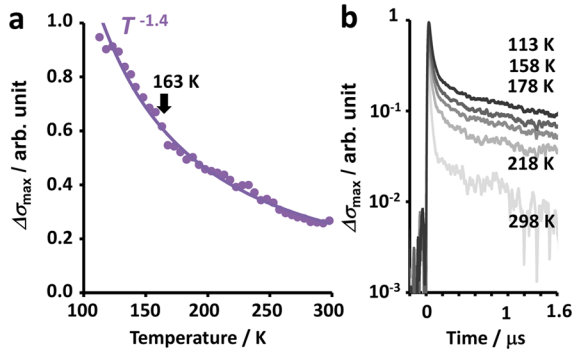

Figure 7. (a) Temperature dependence of the conductivity transient maxima ($\Delta\sigma_{max}$) of PVK/TiO_2 at 9 GHz and $I_0 = 4.6 \times 10^{14}$ photons cm^{-2}; 163 K is the phase transition temperature of PVK (orthorhombic at lower temperatures and tetragonal at higher temperatures). (b) The decay profiles at their respective temperatures.

dependence (all kinetics are given in Supporting Information Figure S6), clearly indicating band-like transport rationalized by phonon scattering ($T^{-3/2}$). Although PVK has a phase transition in the investigated temperature region (being orthorhombic below 162 K and tetragonal from 162 to 327 K),[53] no significant change in the slope was found. Our results were consistent with similar TRMC measurements on PVK/Al_2O_3 (with $T^{-1.7}$) reported by Savenije et al.[54] The indicated band-like transport is in accordance with the observed high local mobility and negligibly small E_T and f_{trap}. Therefore, the excellent photovoltaic properties of PVK/TiO_2 are ensured, in a synergetic manner, by their high charge carrier mobility with band-like transport, low charge recombination rate, low trap density, and shallow trap depth.

3. CONCLUSION

In conclusion, we investigated the dynamics and local transport properties of charge carriers in sequentially deposited $CH_3NH_3PbI_3$ perovskite samples using the TRMC technique. The minimum mobilities at 9 GHz were determined for pure PVK and PVK/TiO_2 (20 $cm^2\ V^{-1}\ s^{-1}$ for both), and for PVK/Al_2O_3 (10 $cm^2\ V^{-1}\ s^{-1}$). On the basis of conductivity quenching by spiro-OMeTAD, we separated the contributions of holes

dx.doi.org/10.1021/ja506936f | J. Am. Chem. Soc. 2014, 136, 13818–13825

and electrons in PVK/TiO_2 (19 and 0.6 $cm^2\ V^{-1}\ s^{-1}$) and PVK/Al_2O_3 (7 and 3 $cm^2\ V^{-1}\ s^{-1}$). The minimum mobilities, $\Sigma\mu_{min}$ were found to generally correlate with the crystal size (70−420 nm) evaluated by AFM, irrespective of the process (one or two-step) and underlying layer (TiO_2 or Al_2O_3). Remarkably, high mobilities of 60−75 $cm^2\ V^{-1}\ s^{-1}$ were revealed at 23 GHz in these composites and explained by band-like transport with a $T^{-1.4}$ dependence due to phonon scattering. Charge recombination in PVK was suppressed by 4−5 orders of magnitude from the Langevin rate, and was further reduced by another order of magnitude in the presence of a mesoporous TiO_2 layer. Analysis of the GHz complex conductivity revealed a very low E_T of 10 meV and f_{trap} of 0.03−0.1 in these PVK frameworks. In addition to the prominent optoelectronic properties of PVK itself, these values were improved by the use of a mesoporous layer, which provided a scaffold on which electronically high-quality crystalline PVK, with a high mobility, a reduced recombination rate, and a low trap density, could be formed. More specifically, whether the scaffold is Al_2O_3 or TiO_2 determines the mobility and dynamics of charge carriers and the energetic landscape of the trap state.

4. EXPERIMENTAL SECTION

4.1. Materials. mp-TiO_2 (300 nm-thick) or mp-Al_2O_3 (220 nm-thick) samples were prepared on a cleaned quartz substrate by spin-coating a diluted TiO_2 or Al_2O_3 paste, followed by sintering at 500 °C for 1 h in a furnace. A perovskite layer was formed either on these mesoporous layers or directly on the quartz by sequential deposition (two step). First, an *N*-*N*′-dimethylformamide (DMF) solution of PbI_2 (99.999% trace metals basis) was spin-coated and immediately annealed at 70 °C for 30 min. Second, the PbI_2 films were dipped into an isopropyl alcohol (IPA) solution of CH_3NH_3I for 20 s, followed by rinsing in fresh IPA for 2 s and annealing at 70 °C for 30 min. The resultant thicknesses of PVK were 260 and 420 nm on mp-TiO_2 and mp-Al_2O_3, respectively. A one-step PVK on the similar mp-TiO_2 or mp-Al_2O_3 was prepared by spin-coating totally 40 wt % DMF solution of CH_3NH_3I and PbI_2 (1:1 molar ratio) followed by heating at 100 °C for 45 min. Subsequently, ca. 150 nm-thick HTL was deposited on the two-step perovskite/mp-TiO_2(or mp-Al_2O_3)/quartz samples by spin-coating a chlorobenzene solution of 2,2′,7,7′-tetrakis(*N*,*N*-di-*p*-methoxyphenyl-amine)9,9′-spirobifluorene (spiro-OMeTAD), 4-*tert*-butylpyridine (TBP), and lithium bis-(trifluoromethylsulfonyl) imide salt (LiTFSI). Further details of the solution contents and preparation conditions including devices are given in the Supporting Information. AFM observations were performed by a Seiko Instruments Inc. model Nanocute OP and Nanonavi II. XRD spectra were measured on a Rigaku MiniFlex600 (Cu Kα: 1.5418 Å) X-ray diffractometer.

4.2. Transient Conductivity. TRMC experiments were carried out using the third harmonic generation (THG; 355 nm) of a Nd:YAG laser (Continuum Inc., Surelite II, 5−8 ns pulse duration, 10 Hz) as an excitation source. X-band (ca. 9.1 GHz), K_u-band (ca. 15.4 GHz), and K-band (ca. 22.9 GHz) microwave circuits equipped with their respective resonant cavities were used to probe the GHz conductivity of all samples. The increase in the reflected microwave power and the negative shift of the resonant frequency of the cavity corresponded to the positive real and negative imaginary conductivities, respectively. Details of this system and the complex conductivity measurements have been previously reported.[32] The experiments were performed at room temperature in air.

■ ASSOCIATED CONTENT

Supporting Information

Experimental details on the fabrication of the solar cells and TRMC samples, decay analysis of the TRMC transients, and frequency dependent analysis by the Drude-Smith/Drude-Zener model, together with Supporting Figures S1−S6. This material is available free of charge via the Internet at http://pubs.acs.org.

■ AUTHOR INFORMATION

Corresponding Authors

saeki@chem.eng.osaka-u.ac.jp
seki@chem.eng.osaka-u.ac.jp

Notes

The authors declare no competing financial interest.

■ ACKNOWLEDGMENTS

This work was supported by a KAKENHI grant from the Ministry of Education, Culture, Sports, Science and Technology (MEXT) of Japan, the Precursory Research for Embryonic Science and Technology (PRESTO) program of the Japan Science and Technology Agency (JST), and a grant from The Murata Science Foundation.

■ REFERENCES

(1) Kojima, A.; Teshima, K.; Shirai, Y.; Miyasaka, T. *J. Am. Chem. Soc.* **2009**, *131*, 6050−6051.
(2) Kim, H.-S.; Lee, C-. R.; Im, J.- H.; Lee, K.- B.; Moehl, T.; Marchioro, A.; Moon, J. S.; Humphry-Baker, R.; Yum, J.- H.; Moser, J. E.; Grätzel, M.; Park, N.-G. *Sci. Rep.* **2012**, *2*, 591/1−591/7.
(3) Lee, M. M.; Teuscher, J.; Miyasaka, T.; Murakami, T. N.; Snaith, H. J. *Science* **2012**, *338*, 643−647.
(4) Snaith, H. J. *J. Phys. Chem. Lett.* **2013**, *4*, 3623−3630.
(5) Park, N.-G. *J. Phys. Chem. Lett.* **2013**, *4*, 2423−2429.
(6) Stranks, S. D.; Eperon, G. E.; Grancini, G.; Menelaou, C.; Alcocer, M. J. P.; Leijtens, T.; Herz, L. M.; Petrozza, A.; Snaith, H. J. *Science* **2013**, *342*, 341−344.
(7) Xing, G.; Mathews, N.; Sun, S.; Lim, S. S.; Lam, Y. M.; Grätzel, M.; Mhaisalkar, S.; Sum, T. C. *Science* **2013**, *342*, 344−347.
(8) Service, R. F. *Science* **2014**, *344*, 458−458.
(9) Liu, M.; Johnston, M. B.; Snaith, H. J. *Nature* **2013**, *501*, 395−398.
(10) Burschka, J.; Pellet, N.; Moon, S.-J.; Humphry-Baker, R.; Gao, P.; Nazeeruddin, M. K.; Grätzel, M. *Nature* **2013**, *499*, 316−319.
(11) Liu, D.; Kelly, T. L. *Nat. Photonics* **2014**, *8*, 133−138.
(12) Heo, J. H.; Im, S. H.; Noh, J. H.; Mandal, T. N.; Lim, C. S.; Chang, A. A.; Lee, Y. H.; Kim, H.-j.; Sarkar, A.; Nazeeruddin, M. K.; Grätzel, M.; Seok, S. I. *Nat. Photonics* **2013**, *7*, 486−491.
(13) Christians, J. A.; Fung, R. C. M.; Kamat, P. V. *J. Am. Chem. Soc.* **2014**, *136*, 758−764.
(14) Ogomi, Y.; Morita, A.; Tsukamoto, S.; Saitho, T.; Fujikawa, N.; Shen, Q.; Toyoda, T.; Yoshino, K.; Pandey, S. S.; Ma, T.; Hayase, S. *J. Phys. Chem. Lett.* **2014**, *5*, 1004−1011.
(15) Eperon, G. E.; Burlakov, V. M.; Docampo, P.; Goriely, A.; Snaith, H. J. *Adv. Funct. Mater.* **2014**, *24*, 151−157.
(16) Chen, Q.; Zhou, H.; Hong, Z.; Luo, S.; Duan, H.-S.; Wang, H.-H.; Liu, Y.; Li, G.; Yang, Y. *J. Am. Chem. Soc.* **2014**, *136*, 622−625.
(17) Liang, P.-W.; Liao, C.-Y.; Chueh, C.-C.; Zuo, F.; Williams, S. T.; Xin, X.-K.; Lin, J.; Jen, A. K.-Y. *Adv. Mater.* **2014**, *26*, 3748−3754.
(18) Even, J.; Pedesseau, L.; Jancu, J.-M.; Katan, C. *J. Phys. Chem. Lett.* **2013**, *4*, 2999−3005.
(19) Giorgi, G.; Fujisawa, J.-I.; Segawa, H.; Yamashita, K. *J. Phys. Chem. Lett.* **2013**, *4*, 4213−4216.
(20) Brivio, F.; Walker, A. B.; Walsh, A. *APL Mater.* **2013**, *1*, 042111/1−042111/5.
(21) Deschler, F.; Price, M.; Pathak, S.; Klintberg, L. E.; Jarausch, D.-D.; Higler, R.; Hüttner, S.; Leijtens, T.; Stranks, S. D.; Snaith, H. J.; Atatüre, M.; Phillips, R. T.; Friend, R. H. *J. Phys. Chem. Lett.* **2014**, *5*, 1421−1426.

(22) Kim, H.-S.; Mora-Sero, I.; Gonzalez-Pedro, V.; Fabregat-Santiago, F.; Juarez-Perez, E. J.; Park, N.-G.; Bisquert, J. *Nat. Commun.* **2013**, *4*, 2242/1−2242/7.
(23) Juarez-Perez, E. J.; Wußler, M.; Fabregat-Santiago, F.; Lakus-Wollny, K.; Mankel, E.; Mayer, T.; Jaegermann, W.; Mora-Sero, I. *J. Phys. Chem. Lett.* **2014**, *5*, 680−685.
(24) Wehrenfennig, C.; Eperon, G. E.; Johnston, M. B.; Snaith, H. J.; Herz, L. M. *Adv. Mater.* **2014**, *26*, 1584−1589.
(25) Marchioro, A.; Teuscher, J.; Friedrich, D.; Kunst, M.; an de Krol, R.; Moehl, T.; Grätzel, M.; Moser, J.-E. *Nat. Photonics* **2014**, *8*, 250−255.
(26) Ponseca, C. S., Jr.; Savenije, T. J.; Abdellah, M.; Zheng, K.; Yartsev, A.; Pascher, T.; Harlang, T.; Chabera, P.; Pullerits, T.; Stepanov, A.; Wolf, J.-P.; Sundström, V. *J. Am. Chem. Soc.* **2014**, *136*, 5189−5192.
(27) Saeki, A.; Koizumi, Y.; Aida, T.; Seki, S. *Acc. Chem. Res.* **2012**, *45*, 1193−1202.
(28) Savenije, T. J.; Murthy, D. H. K.; Gunz, M.; Gorenflot, J.; Siebbeles, L. D. A.; Dyakonov, V.; Deibel, C. *J. Phys. Chem. Lett.* **2011**, *2*, 1368−1371.
(29) Bach, U.; Lupo, D.; Comte, P.; Moser, J. E.; Weissörtel, F.; Salbeck, J.; Spreitzer, H.; Grätzel, M. *Nature* **1998**, *395*, 583−585.
(30) Saeki, A.; Tsuji, M.; Seki, S. *Adv. Energy Mater.* **2011**, *1*, 661−669.
(31) Kroeze, J. E.; Savenije, T. J.; Warman, J. M. *J. Am. Chem. Soc.* **2004**, *126*, 7608−7618.
(32) Saeki, A.; Yasutani, Y.; Oga, H.; Seki, S. *J. Phys. Chem. C* **2014**, DOI: 10.1021/jp505214d.
(33) Poplavskyy, D.; Nelson, J. *J. Appl. Phys.* **2003**, *93*, 341−346.
(34) Ogomi, Y.; Kukihara, K.; Qing, S.; Toyoda, T.; Yoshino, K.; Pandey, S.; Momose, H.; Hayase, S. *ChemPhysChem* **2014**, *15*, 1062−1069.
(35) The electron mobilities at room temperature were calculated by the Einstein relation ($\mu = eD/k_BT$, where e is the electrical charge on an electron, k_B is the Boltzmann constant, D is the diffusion constant, and T is the absolute temperature) using the diffusion constants indicated in the literature, 0.017 $cm^2\ s^{-1}$ in ref 6 and 0.036 $cm^2\ s^{-1}$ in ref 7.
(36) Dualeh, A.; Tétreault, N.; Moehl, T.; Gao, P.; Nazeeruddin, M. K.; Grätzel, M. *Adv. Funct. Mater.* **2014**, *24*, 3250−3258, DOI: 10.1002/adfm.201304022.
(37) Snaith, H. J.; Abate, A.; Ball, J. M.; Eperon, G. E.; Leijtens, T.; Noel, N. K.; Stranks, S. D.; Wang, J. T.-W.; Wojciechowski, K.; Zhang, W. *J. Phys. Chem. Lett.* **2014**, *5*, 1511−1515.
(38) Sanchez, R. S.; Gonzalez-Pedro, V.; Lee, J.-W.; Park, N.-G.; Kang, Y. S.; Mora-Sero, I.; Bisquert, J. *J. Phys. Chem. Lett.* **2014**, *5*, 2357−2363.
(39) Kim, H.-S.; Park, N.-G. *J. Phys. Chem. Lett.* **2014**, *5*, 2927−2934.
(40) Li, N.; Dong, H.; Dong, H.; Li, J.; Li, W.; Niu, G.; Guo, X.; Wu, Z.; Wang, L. *J. Mater. Chem. A* **2014**, *2*, 14973−14978.
(41) Wakamiya, A.; Endo, M.; Sasamori, T.; Tokitoh, T.; Ogomi, Y.; Hayase, S.; Murata, Y. *Chem. Lett.* **2014**, *43*, 711−713.
(42) Cohen, B.-E.; Gamliel, S.; Etgar, L. *APL Mater.* **2014**, *2*, 081502/1−081502/8.
(43) Zhao, Y.; Nardes, A. M.; Zhu, K. *Faraday Discuss.* **2014**, DOI: 10.1039/C4FD00128A.
(44) Haruyama, J.; Sodeyama, K.; Han, L.; Tateyama, Y. *J. Phys. Chem. Lett.* **2014**, *5*, 2903−2909.
(45) Jeon, N. J.; Noh, J. H.; Kim, Y. C.; Yang, W. S.; Ryu, S.; Seok, S. I. *Nat. Mater.* **2014**, *13*, 897−903.
(46) Saeki, A.; Yamamoto, Y.; Koizumi, Y.; Fukushima, T.; Aida, T.; Seki, S. *J. Phys. Chem. Lett.* **2011**, *2*, 2549−2554.
(47) The Langevin rate, k_{Lg}, was given by $k_{Lg} = e(\mu_+ + \mu_-)/(\varepsilon_0\varepsilon_r)$, where ε_0 and ε_r are the dielectric permittivity in a vacuum and the relative permittivity, respectively. The long-range hole and electron mobilities, μ_+ of 0.66 and μ_- of 0.43 $cm^2\ V^{-1}\ s^{-1}$, respectively, were used. These were calculated according to the equation in note. 35 based on the D of ref 6.
(48) Guo, J.; Ohkita, H.; Yokoya, S.; Benten, H.; Ito, S. *J. Am. Chem. Soc.* **2010**, *132*, 9631−9637.
(49) Frost, J. M.; Butler, K. T.; Brivio, F.; Hendon, C. H.; van Schilfgaarde, M.; Walsh, A. *Nano Lett.* **2014**, *14*, 2584−2590.
(50) Savenije, T. J.; Murthy, D. H. K.; Gunz, M.; Gorenflot, J.; Siebbeles, L. D. A.; Dyakonov, V.; Deibel, C. *J. Phys. Chem. Lett.* **2011**, *2*, 1368−1371.
(51) D'Innocenzo, V.; Grancini, G.; Alcocer, M. J. P.; Kandada, A. R. S.; Stranks, S. D.; Lee, M. M.; Lanzani, G.; Snaith, H. J.; Petrozza, A. *Nat. Commun.* **2014**, *5*, 3586/1−3586/6.
(52) Stoumpos, C. C.; Malliakas, C. D.; Kanatzidis, M. G. *Inorg. Chem.* **2013**, *52*, 9019−9038.
(53) Poglitsch, A.; Weber, D. *J. Chem. Phys.* **1987**, *87*, 6373−6378.
(54) Savenije, T. J.; Ponseca, C. S., Jr.; Kunneman, L.; Abdellah, M.; Zheng, K.; Tian, Y.; Zhu, Q.; Canton, S. E.; Scheblykin, I. G.; Pullerits, T.; Yartsev, A.; Sundström, V. *J. Phys. Chem. Lett.* **2014**, *5*, 2189−2194.